

## Chapter 4

# Stress Analysis for Fracture

### 4.1 Introduction

This chapter describes the application of the hybrid phase-shifting full-field experimental CGS-photoelasticity method to fracture studies in a photoelastic material. Section 4.2 presents the theoretical 2D asymptotic crack solution, which is the basis for determining the stress intensity factors for the experimental stress fields, and four cases of stress determination around Mode I-dominant cracks in Homalite-100. Section 4.3 provides some discussion on the use of this experimental method for fracture studies based on the variety of cases presented in this chapter.

### 4.2 Stresses Around Cracks in Homalite-100

#### 4.2.1 2D Asymptotic Crack Solution (Mode I and Mode II)

Assuming that the loaded crack has both symmetric and antisymmetric stress components and that the stresses are characterized by singular terms with constant stress intensity factors  $K_I$  and  $K_{II}$ , the stress field is the sum of the Mode I and Mode II stress field components as follows (Anderson, 2005):

$$\sigma_{xx} = \frac{K_I}{\sqrt{2\pi r}} \cos\left(\frac{\theta}{2}\right) \left[1 - \sin\left(\frac{\theta}{2}\right) \sin\left(\frac{3\theta}{2}\right)\right] - \frac{K_{II}}{\sqrt{2\pi r}} \sin\left(\frac{\theta}{2}\right) \left[2 + \cos\left(\frac{\theta}{2}\right) \cos\left(\frac{3\theta}{2}\right)\right] \quad (4.1a)$$

$$\sigma_{yy} = \frac{K_I}{\sqrt{2\pi r}} \cos\left(\frac{\theta}{2}\right) \left[1 + \sin\left(\frac{\theta}{2}\right) \sin\left(\frac{3\theta}{2}\right)\right] + \frac{K_{II}}{\sqrt{2\pi r}} \sin\left(\frac{\theta}{2}\right) \cos\left(\frac{\theta}{2}\right) \cos\left(\frac{3\theta}{2}\right) \quad (4.1b)$$

$$\sigma_{xy} = \frac{K_I}{\sqrt{2\pi r}} \sin\left(\frac{\theta}{2}\right) \cos\left(\frac{\theta}{2}\right) \cos\left(\frac{3\theta}{2}\right) + \frac{K_{II}}{\sqrt{2\pi r}} \cos\left(\frac{\theta}{2}\right) \left[1 - \sin\left(\frac{\theta}{2}\right) \sin\left(\frac{3\theta}{2}\right)\right]. \quad (4.1c)$$

#### 4.2.2 Calculation of $K_I$ and $K_{II}$ for Mixed-Mode Fracture

The mixed-mode stress intensity factors  $K_I$  and  $K_{II}$  may be determined from the interference patterns of both photoelasticity and CGS, assuming the field of view contains  $K$ -dominant points, i.e., points where the stresses may be characterized by Equation (4.1). From inspiration from Smith and Smith (1972), Sanford and Dally (1979), and Smith and Olaosebikan (1984), who used photoelastic interference patterns, and from Mason et al. (1992), who used CGS interference patterns, an iterative nonlinear least-squares approach using many points from both photoelastic and CGS phase data has been developed for calculating  $K_I$  and  $K_{II}$  for the mixed-mode fracture presented in this chapter.

Since the hybrid method presented in this thesis utilizes two interference techniques, the method for calculating  $K_I$  and  $K_{II}$  naturally includes data from both techniques. The method starts with relationships between the interference phases from both techniques and the variables  $K_I$ ,  $K_{II}$ ,  $r$  and  $\theta$ . Using Equations (3.1) and (4.1), the photoelastic isochromatic phase for mixed-mode  $K$ -dominant fracture is

$$\delta(r, \theta) = \left(\frac{2\pi c_o h}{\lambda}\right) \frac{1}{\sqrt{2\pi r}} \sqrt{[K_I \sin(\theta) + 2K_{II} \cos(\theta)]^2 + [K_{II} \sin(\theta)]^2}, \quad (4.2)$$

and using Equations (2.18a) and (4.1), the CGS phases related to the  $x$  and  $y$  derivatives of the sum of principal stresses for mixed-mode  $K$ -dominant fracture,  $\varphi_{sum}^{\partial x}$  and  $\varphi_{sum}^{\partial y}$ , respectively, are

$$\varphi_{sum}^{\partial x}(r, \theta) = \left(\frac{2\pi \tilde{\Delta} Ch}{p}\right) \frac{1}{\sqrt{2\pi r^3}} \left[-K_I \cos\left(\frac{3\theta}{2}\right) + K_{II} \sin\left(\frac{3\theta}{2}\right)\right] \quad (4.3a)$$

$$\varphi_{sum}^{\partial y}(r, \theta) = \left(\frac{2\pi \tilde{\Delta} Ch}{p}\right) \frac{1}{\sqrt{2\pi r^3}} \left[-K_I \sin\left(\frac{3\theta}{2}\right) - K_{II} \cos\left(\frac{3\theta}{2}\right)\right]. \quad (4.3b)$$

The errors at any point  $i$  for the three phases are dimensionless so that the errors from different types data are comparable and, therefore, may be used in the same nonlinear least-squares algorithm; the errors are defined as the difference between the experimental phases and their theoretical values,

normalized by the range of experimental data of the  $M$  points used in the algorithm for that phase, similar to the NRMSD error measure described in Chapters 2 and 3:

$$\epsilon_i^\delta = \frac{\left[ \delta(r_i, \theta_i) - \left( \frac{2\pi c_0 h}{\lambda} \right) \frac{1}{\sqrt{2\pi r_i}} \sqrt{[K_I \sin(\theta_i) + 2K_{II} \cos(\theta_i)]^2 + [K_{II} \sin(\theta_i)]^2} \right]}{(\max[\delta] - \min[\delta])} \quad (4.4a)$$

$$\epsilon_i^{\partial x} = \frac{\left[ \varphi_{sum}^{\partial x}(r_i, \theta_i) - \left( \frac{2\pi \tilde{\Delta} Ch}{p} \right) \frac{1}{\sqrt{2\pi r_i^3}} \left[ -K_I \cos\left(\frac{3\theta_i}{2}\right) + K_{II} \sin\left(\frac{3\theta_i}{2}\right) \right] \right]}{(\max[\varphi_{sum}^{\partial x}] - \min[\varphi_{sum}^{\partial x}])} \quad (4.4b)$$

$$\epsilon_i^{\partial y} = \frac{\left[ \varphi_{sum}^{\partial y}(r_i, \theta_i) - \left( \frac{2\pi \tilde{\Delta} Ch}{p} \right) \frac{1}{\sqrt{2\pi r_i^3}} \left[ -K_I \sin\left(\frac{3\theta_i}{2}\right) - K_{II} \cos\left(\frac{3\theta_i}{2}\right) \right] \right]}{(\max[\varphi_{sum}^{\partial y}] - \min[\varphi_{sum}^{\partial y}])}. \quad (4.4c)$$

The normalization is done by the range of the experimental data instead of the theoretical data in order to avoid dividing the differences between the experimental and theoretical phases by zero.

Since the experimental phases used in the error calculations come from an unwrapping process that incorporates a data-quality weight function given by Equation (2.28), the errors  $\epsilon_i^\delta$ ,  $\epsilon_i^{\partial x}$ , and  $\epsilon_i^{\partial y}$  are multiplied by the appropriate weight functions calculated for the PCG unwrapping algorithm for every point  $i$ , such that the higher quality data points receive more weight in the least-squares minimization algorithm. The weight functions for the isochromatic phase and the CGS phases related to the  $x$  and  $y$  derivatives of  $\sigma_1 + \sigma_2$  are denoted  $W_i^\delta$ ,  $W_i^{\partial x}$ , and  $W_i^{\partial y}$ , respectively.

The iterative nonlinear least-squares algorithm minimizes the function  $f(K_I, K_{II})$ , which is a vector function incorporating these error definitions and appropriate weight functions described above, by iteratively choosing  $K_I$  and  $K_{II}$  values using the trust-region-reflective algorithm based on the interior-reflective Newton method, which is a standard nonlinear least-squares algorithm; this algorithm has been implemented in MATLAB<sup>®</sup>. The function  $f(K_I, K_{II})$  and the minimization of the squared  $L_2$  norm is as follows, for  $M$  points of  $\delta$ ,  $N$  points of  $\varphi_{sum}^{\partial x}$ , and  $P$  points of  $\varphi_{sum}^{\partial y}$ :

$$\mathbf{f}(K_I, K_{II}) = \left[ \frac{1}{\sqrt{2}} W_1^\delta \epsilon_1^\delta, \dots, \frac{1}{\sqrt{2}} W_M^\delta \epsilon_M^\delta, \frac{1}{2} W_1^{\partial x} \epsilon_1^{\partial x}, \dots, \frac{1}{2} W_N^{\partial x} \epsilon_N^{\partial x}, \frac{1}{2} W_1^{\partial y} \epsilon_1^{\partial y}, \dots, \frac{1}{2} W_P^{\partial y} \epsilon_P^{\partial y} \right]^T \quad (4.5)$$

$$\begin{aligned} \min_{K_I, K_{II}} \left\| \mathbf{f}(K_I, K_{II}) \right\|_2^2 &= \min_{K_I, K_{II}} (f_1^2 + f_2^2 + \dots + f_{M+N+P}^2) \\ &= \min_{K_I, K_{II}} \left( \frac{1}{2} \sum_{i=1}^M (W_i^\delta \epsilon_i^\delta)^2 + \frac{1}{4} \sum_{j=1}^N (W_j^{\partial x} \epsilon_j^{\partial x})^2 + \frac{1}{4} \sum_{k=1}^P (W_k^{\partial y} \epsilon_k^{\partial y})^2 \right). \end{aligned} \quad (4.6)$$

The constant coefficients in front of the elements of the vector function  $\mathbf{f}$  in Equation (4.5) and the constants in front of the summation symbols of Equation (4.6) are present to equally weight the contributions of the two experimental techniques to the minimization algorithm since photoelasticity gives only one stress-related phase and CGS gives two, i.e., the photoelasticity data set receives twice the weight in the minimization algorithm as each of the CGS data sets.

Another consideration in the determination of  $K_I$  and  $K_{II}$  is the assumption of plane stress in these specimens; the mixed-mode fracture stress fields in Equation (4.1) are only valid for plane stress K-dominant regions. The stresses determined by transmission interference techniques are inherently through-thickness averages of the stresses, so if the specimen is under plane stress, then the measured stresses are constant through the thickness. Since the field of view is small in cases presented here, a notable portion of the field of view of the interference patterns are subject to 3D (triaxial) stress effects around the crack tip, meaning the stresses measured in this region vary through the thickness and are not purely plane stress. According to Rosakis et al. (1990) and Krishnaswamy et al. (1991), who studied 3D effects in elastodynamic crack problems, the extent of the 3D zone has a radius around  $0.4\text{--}0.5h$ . Using this as a general guideline for excluding points in the field of view that may be subject to 3D effects, all of the points inside a circle of radius  $0.5h$  centered around the crack tip are excluded from the points used in calculating  $K_I$  and  $K_{II}$ . Additionally, all points that have been excluded by a user-defined mask in the unwrapping algorithm are also excluded from consideration. In the spirit of having full-field phase maps, all the points not excluded for the three phases in the field of view are used in the nonlinear least-squares minimization algorithm to determine  $K_I$  and  $K_{II}$ .

### 4.2.3 Wedge Opening Experiments: Mode I–Dominant Cracks

The experimental loading configuration is a symmetric wedge with an angle  $2\chi = \pi/9$  symmetrically opening a straight notch of length  $a_1$  that is at the tip of a V-shaped notch and that has a sharp crack of length  $a_2$  emanating from the straight notch tip, as shown in Figure 4.1(a). The sharp crack is formed from two steps. First, a straight razor blade is pressed into the tip of the straight notch, initiating two sharp, short, crack-like defects, one on each face of the specimen moving partly through the thickness. Second, the loading condition for the experiments is used to gently and slowly open the notch to fill in the crack through-thickness from these two defects as shown in Figure 4.1(b); the crack generally propagates and then arrests a few millimeters from the straight notch tip. Fast loading of this notch leads to sudden and complete fracture of the specimen, so modest displacement rates of the wedge around  $50 \mu\text{m/s}$  produces cracks that do not propagate the length of the specimen. The specimen is then unloaded before the experimental loads to adjust the specimen height such that the crack tip is in the field of view of the optical setup. This precracking method is useful for brittle photoelastic materials, but may be less successful in ductile photoelastic materials because the defects made by the razor blade do not coalesce when wedged open in ductile materials.

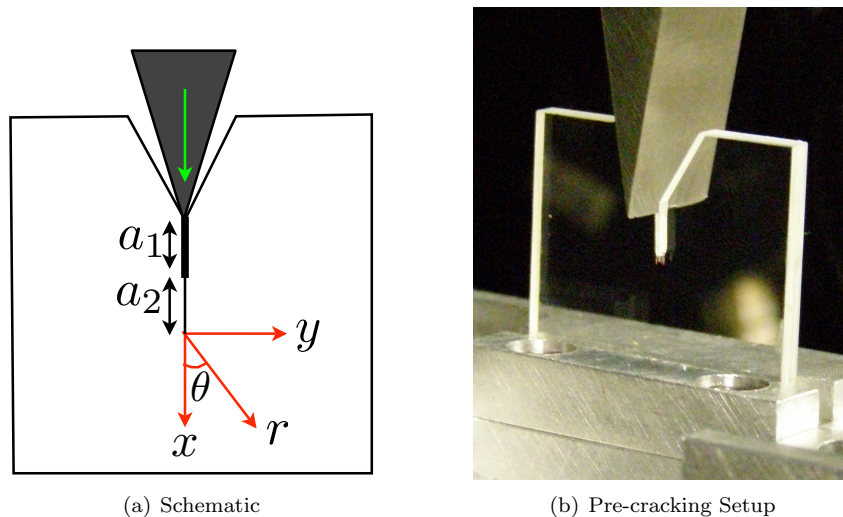


Figure 4.1: Experimental loading configuration for wedge opening

During experimental loading, the wedge can be slightly misaligned with the  $x$  axis, and therefore the downward motion of the wedge can impart a slight Mode II load to the crack, evident in slight asymmetry in the stress fields. Another possibility for a Mode II contribution to the stress field is the symmetric Mode I loading of a crack with a slight angle  $\beta_c$  to the  $x$  axis (Anderson, 2005). With these experiments, the theoretical model is a straight crack along the  $x$  axis with superposed dominant Mode I and slight Mode II loadings. The level of mode-mixity is characterized by the stress intensity factor ratio  $\mu_{SIF} = K_{II}/K_I$ . In these experiments, the translating mirror setup is used instead of the non-polarizing beamsplitter to remove possible errors due to the transmission and reflectance coefficients of the beamsplitter. Use of a beamsplitter with well-matched coefficients should not change the applicability of this experimental method to fracture studies.

#### 4.2.4 Crack with $K_I = 0.514 \text{ MPa}\sqrt{\text{m}}$ and $K_{II} = 4.4 \text{ kPa}\sqrt{\text{m}}$

In specimen called HomC1, the material is Homalite-100, with thickness of  $h = 2.19 \text{ mm}$ , outer dimensions  $25.48 \text{ mm} \times 25.48 \text{ mm}$ , V-notch depth of  $6.25 \text{ mm}$ , straight notch length of  $a_1 = 4.01 \text{ mm}$  and crack length of  $a_2 = 4.05 \text{ mm}$ . The material properties of Homalite-100 are Young's modulus  $E = 4.55 \text{ GPa}$ , refractive index  $n_o = 1.561$ , Poisson's ratio  $\nu = 0.31$ , photoelastic constants  $A = -9.058 * 10^{-11} \text{ m}^2/\text{N}$ ,  $B = -1.143 * 10^{-10} \text{ m}^2/\text{N}$ ,  $C = -1.41 * 10^{-10} \text{ m}^2/\text{N}$ , and  $g = -0.0844$  (RaviChandar, 1982; Kobayashi, 1993). The optical field of view imaged onto the sensor is  $4.60 \text{ mm} \times 4.60 \text{ mm}$ , and the image resolution is  $4.6 \mu\text{m}$ . For this CGS setup, the Ronchi grating pitch is  $p = 1 \text{ mm}/40$ ; the grating separation is  $\tilde{\Delta} = 8.87 \text{ mm}$ ; the wavelength of light from the linearly polarized HeNe laser is  $\lambda = 632.8 \text{ nm}$ ; and the resulting lateral shearing distance is  $d_{shear} = 225 \mu\text{m}$ . Figure 4.2.4 shows the specimen before loading with the experimental field of view indicated on the specimen. The measured stresses in this small field of view indicate local through-thickness average stress information around the crack tip.

$K_I$  and  $K_{II}$  values of  $0.514 \text{ MPa}\sqrt{\text{m}}$  and  $4.4 \text{ kPa}\sqrt{\text{m}}$  are determined for this load case from by using the least-squares algorithm described in Section 4.2.2. This specimen HomC1 has the highest  $K_I$  of all the loadings of similar configurations. The  $K_{II}$  component is small with a stress

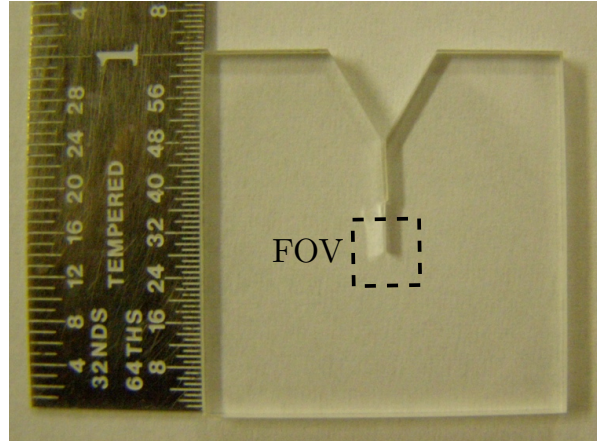


Figure 4.2: Specimen HomC1 before loading with field of view (FOV) indicated

intensity factor ratio  $\mu_{SIF} = 0.0085$ , so the dominant features of the stress field are Mode I, which is symmetric about the  $x$  axis.

The static initiation fracture toughness  $K_{Ic}$  values for Homalite-100 vary in literature and can vary for the same set of experiments. Bradley and Kobayashi (1971) reported fracture toughness values ranging from  $0.593 \text{ MPa}\sqrt{\text{m}}$  to  $0.690 \text{ MPa}\sqrt{\text{m}}$  with an average of  $0.636 \text{ MPa}\sqrt{\text{m}}$ . Irwin et al. (1979) and Dally (1979) state that Bradley and Kobayashi (1971) overestimates the initiation fracture toughness and report a value of only  $0.445 \text{ MPa}\sqrt{\text{m}}$ . The calculated  $K_I$  value for this load is around the reported fracture toughness values; since the next load increment during this experiment caused crack propagation, the measured  $K_I$  value seems reasonable to be close to reported fracture toughness values.

The experimental data is compared to theoretical data from the average  $K_I$  and  $K_{II}$  values. The main differences arise from errors in the isoclinic angle, which is highly dependent on the alignment of the polarization optics, as explained in Chapter 3, and due to the breakdown in the derivative approximation of the CGS data near the crack tip where the fringe density is high.

Given the experimental configuration, the optical coordinate system is the  $\pi/2$  rotation of the conventional crack-plane coordinate system. Due to possible confusion, in this chapter, the  $x$  and  $y$  axes refer to the crack-plane coordinate systems, the variables defined in the optical coordinate system in previous chapters retain their original meaning in reference to the optical coordinate

system (such as  $E_x\hat{i}$  is the optical- $x$  component of the electric field, and vertical shearing CGS is shearing in the optical- $y$  axis), and any other possible confusion is clearly denoted as either relative to the optical or specimen coordinate systems.

#### 4.2.4.1 Experimental and Theoretical Phase-Shifted Interference Images

Figures 4.3 and 4.4 show the experimental and theoretical six phase-shifted photoelasticity images for specimen HomC1. The features of the experimental images match remarkably well with the theoretical images, taking into account for the slightly Gaussian behavior of the background intensity field  $I_o$  in the experimental images as opposed to the uniform theoretical  $I_o$ . The experimental images also appear to have similar high-frequency, low-amplitude undulation on top of the underlying photoelastic fringes as was present in the polycarbonate data in Figure 3.3 in Chapter 3. These undulations are Fizeau fringes. This noise source is minimized using a Wiener filter with window size of  $[25 \times 25]$  pixels before processing the data. As expected, the high stresses at the crack tip result in caustic shadows in the experimental images; these caustic shadows are not modeled in the theoretical fields. The caustic shadows are present in all of the experimental images for both experimental techniques in the data presented in this chapter because the imaging method used in the experiment is unable to capture the divergent light rays at the crack tip for these cases.

Figures 4.5–4.10 are the experimental and theoretical image sets of four phase-shifted images for vertical shear CGS for the pure  $E_x\hat{i}$  input, pure  $E_y\hat{j}$  input, and circularly polarized electric field input from the  $\lambda/4$  polarization method. Since Homalite-100 has a modest value for  $g$  of  $-0.0844$ , which dictates the relative strength of secondary CGS phase  $\varphi_{diff}$  related to  $\sigma_1 - \sigma_2$ , then  $\varphi_{sum}$  phase dominates the images for each of the different electric field inputs. The difference between the images from the various polarization states of the input electric field are rather subtle. The images from the circularly polarized field (Figures 4.9 and 4.10) have the dominant circular features of  $\varphi_{sum}$  with some slight modulation of the intensity near the crack tip where  $\cos(\varphi_{diff})$  is close to zero. (Figure 4.22(f) shows that the  $\cos(\varphi_{diff})$  field is fairly uniform and close to a value of 1 except near the crack). Both the experimental and theoretical images from pure  $E_x\hat{i}$  input (Figures 4.5

and 4.6) are elongated along the vertical optical direction, while the images from the pure  $E_y\hat{i}$  input (Figures 4.7 and 4.8) are elongated along the horizontal optical direction, as compared to the images from the circularly polarized input case in Figures 4.9 and 4.10). Overall, the experimental images tend to be stretched along the shearing direction as compared to the theoretical images because the experimental phases, which approximately relate to the derivatives of stress, cannot capture the large changes in the derivatives of stress near the crack tip with a finite shearing distance  $d_{shear} = 225 \mu\text{m}$  that is 5% of the field of view. Despite this finite shearing distance, the experimental and theoretical images compare well in fringe density, shape, and contrast.

Figures 4.11–4.16 are the experimental and theoretical image sets of four phase-shifted images for horizontal shear CGS for the pure  $E_x\hat{i}$  input, pure  $E_y\hat{j}$  input, and circularly polarized electric field input from the  $\lambda/4$  polarization method. As with the vertical shear, the experimental images compare well with the theoretical images, with slight differences near the crack tip due to the finite shearing distance issue described above. The circularly polarized light result in the expected circular lobes to the side of the crack in Figures 4.15 and 4.16, while the pure  $E_x\hat{i}$  and  $E_y\hat{j}$  inputs result in slightly elongated fringes along the vertical and horizontal optical directions, respectively. The finite shearing distance is visible in the horizontal shear; the crack appears to be doubled in the experimental images. Data points between the crack are not reliable because these arise from interference of light on opposite sides of the crack, and therefore this data is masked in the analysis.